

Theory of Non-Dichroic Enantio-Sensitive Chiroptical Spectroscopy

Andrés Ordóñez^{1,*}, David Ayuso², Piero Decleva³, Letizia

Fede⁴, Debobrata Rajak⁵, Yann Mairesse⁴, and Bernard Pons^{4†}

¹ *Department of Physics, Freie Universität Berlin, 14195 Berlin, Germany*

² *Department of Chemistry, Molecular Sciences Research Hub, Imperial College London, SW7 2AZ London, UK*

³ *Università degli Studi di Trieste, Trieste, Italy*

⁴ *Université de Bordeaux – CNRS – CEA, CELIA, UMR5107, Talence, France and*

⁵ *ELI ALPS, The Extreme Light Infrastructure ERIC, Wolfgang Sandner u. 3., 6728 Szeged, Hungary*

We show that the photoelectron angular distributions produced by elliptical and cross-polarized two-color laser fields interacting with randomly oriented chiral molecules decompose into four irreducible representations of the D_{2h} point group. One of these (A_u) corresponds to a non-dichroic enantiosensitive (NoDES) contribution. This NoDES contribution has opposite sign for opposite enantiomers but remains invariant under reversal of the field ellipticity, enabling chirality detection that is robust against variations of the relative phase between orthogonal field components. We propose a protocol to isolate this component using only two velocity-map imaging projections and validate it through numerical simulations. Our calculations, performed in the two-photon resonantly-enhanced ionization, multi-photon, and strong-field ionization regimes with cross-polarized two-color fields show that the NoDES signal reaches about 1% of the energy-resolved ionization yield, comparable to photoelectron circular dichroism and much larger than standard magnetic-dipole chiroptical effects. NoDES spectroscopy thus provides a symmetry-protected and phase-robust route to probe molecular chirality on the ultrafast time scale. The experimental confirmation of our theory is presented in the companion paper [L. Fede *et al.*, arXiv (2025)].

I. INTRODUCTION

The interaction of chiral molecules with elliptically or circularly polarized light produces a variety of chiroptical effects [1], such as circular dichroism (CD), circularly polarized luminescence [2], magnetochiral circular dichroism [3], and photoelectron circular dichroism (PECD) [4–6], to name a few. Among them, PECD stands out for two reasons: (i) it reaches high chiral/achiral signal ratios ($\sim 10\%$) at the single-molecule level, making it the tool of choice to investigate the time-resolved dynamics of chiral molecules [7, 8] and (ii) it provides direct access to tensorial observables via the multipolar expansion of the photoelectron angular distribution (PAD) $P(\theta, \phi) = \sum_{l,m} b_{l,m} Y_{l,m}(\theta, \phi)$. The essence of PECD is that photoionization of randomly oriented molecules using circularly polarized light produces a forward-backward asymmetry (FBA), encoded in the odd- l $b_{l,0}$ coefficients. These odd- l coefficients, which emerge already within the electric-dipole approximation and are rather sensitive to the molecular structure, change sign upon reversal of either the molecular chirality (enantiosensitivity) or the rotation direction of the light polarization (circular dichroism). The simultaneous enantiosensitive and dichroic behavior is a consequence of symmetry; it follows from how the sample, the polarization of the electric field, and the odd- l spherical harmonics transform with respect to rotations and reflec-

tions. Being rooted in symmetry, PECD is observable across a wide range of molecular species [6, 9], ionization regimes [10], and pulse durations [11].

PECD was initially experimentally investigated using single-photon ionization by XUV radiation [9, 12]. Later on, it was extended to the multiphoton regime using UV femtosecond laser pulses [13, 14], and to the strong-field ionization regime using IR laser pulses [10]. Accessing the multiphoton and strong-field regimes opened the door to a rich playground in which multiple laser pulses, with various polarization states, can be combined to measure and control the photoionization process [15–21], as well as to optimize the chiral response [22]. In particular, the nonlinear regime provides access to $b_{l,m}$ coefficients which are absent in the one-photon case due to selection rules.

Selection rules have their origin in symmetries, which can be of geometric or dynamic character. Geometric selection rules (e.g. $b_{l,m \neq 0} = 0$ for circularly polarized light due to cylindrical symmetry) are valid independently of the number of photons absorbed in the ionization process. They simply reflect Curie’s principle: the output (PAD) must be as symmetric as the input (sample + polarization). In contrast, dynamical selection rules (e.g. $b_{l,m} = 0$ for $l > 2N$, where N is the number of absorbed photons) result from the structure of the integrals describing the specific absorption process. By moving beyond circular polarization and one-photon absorption, both geometrical and dynamical selection rules can be broken, leading to new $b_{l,m}$ coefficients. For example, although elliptically polarized light $\vec{E}(t) = E[\cos(\omega t)\hat{x} + \varepsilon \sin(\omega t)\hat{y}]$ breaks cylindrical sym-

* andres.ordonez@fu-berlin.de

† bernard.pons@u-bordeaux.fr

metry, $b_{2,-2}$ ($Y_{2,-2} \propto \sin^2 \theta \sin 2\phi$, we use real-valued spherical harmonics) remains forbidden by a dynamical symmetry in the one-photon case (see e.g. Ref. [23]). This dynamical symmetry is broken in the multiphoton case, where $b_{2,-2}$ and other l -even $b_{l,m<0}$ coefficients lead to elliptically dichroic azimuthal offsets of the PAD in atoms [24–34] and molecules [35].

Over the last decade, the role of elliptically polarized light in photoelectron dichroism has attracted growing attention, leading to the emergence of photoelectron elliptical dichroism (PEELD). In contrast to the one-photon ionization regime, where the FBA depends linearly on the normalized Stokes parameter $S_3/S_0 = 2\varepsilon/(1 + \varepsilon^2)$, in the multiphoton regime this dependence can be non-linear [36, 37] and even non-monotonic [38–40], providing valuable information about the intermediate resonances in the multiphoton ionization pathway [41] and thus enhanced molecular specificity [42]. Furthermore, besides odd- l $b_{l,0}$ coefficients, recent experiments have reported non-negligible odd- l $b_{l,m>0}$ coefficients that are enantiosensitive and elliptically dichroic [39].

Since $b_{l,m \neq 0}$ coefficients describe modulations in the azimuthal angle ϕ [$Y_{l,m<0} \propto \sin(m\phi)$, $Y_{l,m>0} \propto \cos(m\phi)$], they may be lost when taking a single projection of the PAD using a velocity-map imaging spectrometer (VMI) [43], as is common in PECD and PEELD studies. For example, $\cos \phi \propto p_x$ is washed out when projected along the x axis. Indeed, the emergence of $b_{l,m \neq 0}$ coefficients rules out the possibility of a full reconstruction of all $b_{l,m}$ coefficients from a single projection [39]. Complete reconstructions can be achieved via direct 3D momentum imaging [38, 44, 45] or through tomographic imaging from multiple projections [36, 38, 46–48]. Nevertheless, as we will show, a pair of projections along judiciously chosen directions are enough to reveal the object of interest in this work, the non-dichroic enantiosensitive (NoDES) signal.

Enantiosensitive and dichroic $b_{l,m \neq 0}$ coefficients have also emerged in photoionization with orthogonal ω - 2ω fields $\vec{E}(t) = E_\omega \cos(\omega t)\hat{x} + E_{2\omega} \cos(2\omega t + \varphi)\hat{y}$ [16, 19, 49–52]. These coefficients describe forward-backward up-down asymmetries, i.e. asymmetries such as a $Y_{2,1} \propto p_x p_z$ quadrupole. Such asymmetries become evident upon projection of the PAD along the 2ω polarization direction. An intuitive approach to analyze this type of asymmetry relies on how $\vec{E}(t)$ rotates in opposite directions when $E_x(t) > 0$ and when $E_x(t) < 0$ [16, 49]. However, the shape and magnitude of the forward-backward up-down asymmetry depend on the phase φ between the two frequency components of the field (see Sec. VI), as well as on the phases inherent to ω and 2ω transition amplitudes [50]. In spite of this, and from a general point of view, the C_{2y} (rotation by 180° around the y axis) symmetry of the field requires any FBA along z to be accompanied by an up-down asymmetry along x . Further symmetry analysis of this field reveals the selection rules governing which $b_{l,m}$ coefficients are al-

lowed, which ones are enantiosensitive, and which ones are dichroic (i.e. change sign upon $\varphi \rightarrow \varphi + \pi$) [52]. Surprisingly, besides $b_{l,m}$ coefficients that are enantiosensitive and dichroic (e.g. $b_{2,1}$), the symmetry analysis predicts a class of $b_{l,m}$ coefficients that are enantiosensitive but non dichroic. An example is $b_{3,-2}$, which yields an octupolar asymmetry $Y_{3,-2} \propto p_x p_y p_z$, and is predicted to emerge upon absorption of one photon at ω plus one photon at 2ω . This asymmetry is washed out upon projection of the PAD along the 2ω polarization direction (the most common configuration), but should be visible when projecting along the bisector direction of the two ionizing polarizations [52]. An analogous symmetry analysis reveals that such non-dichroic enantio-sensitive (NoDES) $b_{l,m}$ coefficients also appear for elliptically polarized light. However, dynamical symmetries rule them out at least in one- and two-photon ionization [52].

Reference [52] provided an analytical expression for the lowest- l NoDES coefficient $b_{3,-2}$ in the case of two-photon ionization with orthogonal ω - 2ω fields. However the value of $b_{3,-2}$, or of any other NoDES $b_{l,m}$ coefficient in any ionization regime has not been reported yet. In a companion letter [53], we report on measurement of NoDES signals in the multiphoton and strong-field ionization of chiral molecules by elliptically and orthogonal ω - 2ω laser fields. In this article, we provide the theoretical framework for NoDES spectroscopy.

In Sec. II, we derive the selection rules for the observation of NoDES $b_{l,m}$ terms in multiphoton ionization by a monochromatic elliptical laser field. Section III describes the derivation of these rules for orthogonal two-color laser fields. Section IV shows how the NoDES signal can be extracted using a pair of VMI projections. In Sec. V, we present simulations of NoDES signals in two-photon ionization of methyloxirane by cross polarized, two-color fields. Section VI describes calculations in the multiphoton and strong field regimes on a toy-model chiral molecule. Finally, Sec. VII summarizes our conclusions.

II. SELECTION RULES FOR ELLIPTICAL FIELDS

The PAD $P(\theta, \phi)$ resulting from the interaction between an elliptically polarized electric field

$$\vec{E}(t) = E_0 [\cos(\omega t)\hat{x} + \varepsilon \sin(\omega t)\hat{y}], \quad (1)$$

with a randomly oriented sample of chiral molecules can be split into four contributions:

$$P = P_{NN} + P_{YY} + P_{NY} + P_{YN} \quad (2)$$

where the first subindex (Y for Yes, N for No) designates enantiosensitivity, and the second subindex dichroism. That is, P_{NN} is neither enantiosensitive nor dichroic, P_{YY} is both enantiosensitive and dichroic, P_{NY} is not enantiosensitive but is dichroic, and P_{YN} is enantiosensitive but not dichroic. P_{YN} is the NoDES signal.

Each contribution in Eq. (2) is either even or odd with respect to C_{2x} (rotation by 180° around the x axis) and σ_{xy} (reflection in the xy plane) as shown in Table I. This is because, in the electric-dipole approximation and for randomly oriented molecules, C_{2x} reverses the ellipticity without changing the enantiomer, while σ_{xy} reverses the enantiomer without changing the field. Furthermore, the PAD must exhibit the joint symmetry of the light-matter system and thus it must be invariant with respect to C_{2z} .

The operators C_{2z} , C_{2x} and σ_{xy} generate the D_{2h} group. Each contribution to P in Eq. (2) corresponds to a certain irreducible representation of D_{2h} , as indicated in parentheses in Table I. In particular, the NoDES signal corresponds to the A_u irreducible representation of D_{2h} . One can extract each of the four contributions $P_{\text{irrep}} = P_{NN}, P_{YY}, P_{NY}, P_{YN}$ by appropriate projection

$$P_{\text{irrep}} = \frac{1}{2^3} [1 + \chi_{\text{irrep}}^{\sigma_{xy}} \sigma_{xy}] [1 + \chi_{\text{irrep}}^{C_{2x}} C_{2x}] [1 + C_{2z}] P \quad (3)$$

where $\chi_{\text{irrep}}^{\sigma_{xy}}$ and $\chi_{\text{irrep}}^{C_{2x}}$ are the characters associated to the corresponding contribution (irreducible representation).

Having identified the relevant irreducible representations of the PAD, it can be expressed in any symmetry-adapted basis to clearly identify the signals according to their enantioselectivity and dichroism. For expansions in terms of real spherical harmonics,

$$P(\theta, \phi) = \sum_{l,m} b_{l,m} Y_{l,m}(\theta, \phi), \quad (4)$$

one can use $C_{2z} Y_{l,m} = (-1)^m Y_{l,m}$, $\sigma_{xy} Y_{l,m} = (-1)^{l+m} Y_{l,m}$, $C_{2x} Y_{l,m} = (-1)^{l+m} Y_{l,m}$ if $m \geq 0$, and $C_{2x} Y_{l,m} = (-1)^{l+m+1} Y_{l,m}$ if $m < 0$ to assign each $Y_{l,m}$ to the corresponding irreducible representation. The $b_{l,m}$ coefficients transform accordingly. This leads to the last two columns of Table I, which provide selection rules for enantioselectivity and dichroism of the $b_{l,m}$ coefficients. In particular, the NoDES signal is encoded in the $b_{l,m}$ coefficients with odd l and negative, even m . Table II lists the enantioselectivity and dichroism of $b_{l,m}$ coefficients with $l \leq 9$, which have been experimentally verified in the companion paper [53].

For circular polarization, $|\varepsilon| = 1$, and we must replace $C_{2,z}$ by $C_{\infty,z} = \{C_\phi | \phi = [0, 2\pi)\}$, the set of all rotations around z . Thus we deal with $D_{\infty h}$ instead of D_{2h} . According to the correlation between the irreducible representations of $D_{\infty h}$ and D_{2h} ($\Sigma_g^+ \leftrightarrow A_g$, $\Sigma_u^+ \leftrightarrow B_{1u}$, $\Sigma_g^- \leftrightarrow B_{1g}$, $\Sigma_u^- \leftrightarrow A_u$), for circular polarization $P_{NN} = \Sigma_g^+$, $P_{YY} = \Sigma_u^+$, $P_{NY} = \Sigma_g^-$, $P_{YN} = \Sigma_u^-$. It is easy to see that Σ_g^- and Σ_u^- cannot be represented using single-particle functions, like spherical harmonics, and thus there is neither a P_{NY} nor a P_{YN} contribution in this case. Indeed, since cylindrical symmetry only allows $m = 0$, the effect of σ_{xy} and C_{2x} on the allowed spherical harmonics is identical, i.e. $\sigma_{xy} Y_{l,0} = C_{2x} Y_{l,0} = (-1)^l Y_{l,0}$. Thus enantioselectivity and dichroism are represented by the same (odd- l) harmonics. This ‘‘degeneracy’’ is lifted in the less symmetric D_{2h} group, which

	σ_{xy}	C_{2x}	C_{2z}	l	m
$P_{NN} (A_g)$	1	1	1	even	even, ≥ 0
$P_{YY} (B_{1u})$	-1	-1	1	odd	even, ≥ 0
$P_{NY} (B_{1g})$	1	-1	1	even	even, < 0
$P_{YN} (A_u)$	-1	1	1	odd	even, < 0

Table I. Character table for the different contributions to the PAD [Eq. (2)] resulting from photoionization of randomly oriented chiral molecules using elliptically polarized light [Eq. (1)]. The first subindex of P indicates enantioselectivity and the second dichroism (Y=Yes, N=No). The corresponding irreducible representations belonging to the group D_{2h} are shown in parenthesis. The last two columns show the conditions on l and m for real spherical harmonics Y_l^m belonging to each irreducible representation. These provide the selection rules for enantioselectivity and dichroism of the corresponding $b_{l,m}$ coefficients [Eq. (4)].

$l \backslash m$	-8	-6	-4	-2	0	2	4	6	8
0					NN				
1					YY				
2				NY	NN	NN			
3				YN	YY	YY			
4			NY	NY	NN	NN	NN		
5			YN	YN	YY	YY	YY		
6		NY	NY	NY	NN	NN	NN	NN	
7		YN	YN	YN	YY	YY	YY	YY	
8	NY	NY	NY	NY	NN	NN	NN	NN	NN
9	YN	YN	YN	YN	YY	YY	YY	YY	YY

Table II. Enantioselectivity (Y=Yes, N=No) and dichroism (Y/N) of the $b_{l,m}$ coefficients [see Eq. (4) and Table I] obtained upon ionization of randomly oriented chiral molecules with elliptically polarized light for $l \leq 9$ [Eq. (1)]. See experimental confirmation in the companion paper [53].

allows for $m \neq 0$, and different transformation rules for $Y_{l,m}$ under σ_{xy} and C_{2x} .

Interestingly, the P_{NY} and P_{YN} contributions could emerge for circular polarization when additional degrees of freedom are resolved (e.g. electron and ion, or electron momentum and spin, in coincidence). In this case the PAD can be expanded in terms of two-particle functions, namely coupled spherical harmonics $\mathcal{Y}_{L,M=0}^{l_1 l_2}(\theta_1, \phi_1; \theta_2, \phi_2)$. Their transformation rules with respect to σ_{xy} and C_{2x} allow for P_{NY} and P_{YN} (NoDES) contributions – see Ref. [54] for a related discussion in the context of recoil-frame photoelectron angular distributions in one-photon ionization with unpolarized light. We remark that detecting two-particle angular distributions [55] is considerably more demanding than the single-particle case discussed here and that the presence of NoDES contributions in that context has not been verified experimentally yet.

	σ_{xy}	C_{2x}	C_{2y}	l	m
$P_{NN} (A_g)$	1	1	1	even	even, ≥ 0
$P_{YY} (B_{2g})$	-1	-1	1	even	odd, ≥ 0
$P_{NY} (B_{2u})$	1	-1	1	odd	odd, < 0
$P_{YN} (A_u)$	-1	1	1	odd	even, < 0

Table III. Same as Table I but for photoionization with an orthogonal two-color field [Eq. (5)].

III. SELECTION RULES FOR ORTHOGONAL TWO-COLOR FIELDS

In the case of an orthogonal two-color field

$$\vec{E}(t) = E_0 [\cos(\omega t)\hat{x} + r \cos(2\omega t + \varphi)\hat{y}], \quad (5)$$

we can also express the PAD as in Eq. (2). In this case, the light-matter system is invariant with respect to C_{2y} instead of C_{2z} , and dichroism is understood as a change of sign upon $\varphi \rightarrow \varphi + \pi$. P_{NN} and P_{YN} remain the same as in the elliptical case, while P_{YY} and P_{NY} now correspond to the B_{2g} and B_{2u} irreducible representations, respectively, as shown in Table III. The conditions on l and m are obtained using $C_{2y}Y_{l,m} = (-1)^l Y_{l,m}$ if $m \geq 0$ and $C_{2y}Y_{l,m} = (-1)^{l+1} Y_{l,m}$ if $m < 0$. Note that since the NoDES signal is again encoded in the A_u irreducible representation, the corresponding $b_{l,m}$ coefficients are the same as in the elliptical case. The projector on a given irreducible representation P_{irrep} can be obtained by replacing $C_{2z} \rightarrow C_{2y}$ in Eq. (3). Table IV lists the enantioselectivity and dichroism of $b_{l,m}$ coefficients with $l \leq 9$, which are numerically verified in Sec. VI. Experimental evidence of the presence of the NoDES signal (P_{YN}) for this field, obtained using the approach presented in the next section, is presented in the companion paper [53].

IV. EXTRACTING THE NODES SIGNAL USING TWO VMI PROJECTIONS

As shown in previous sections, the NoDES signal is encoded in the A_u irreducible representation of D_{2h} , which corresponds to $b_{l,m}$ coefficients with odd l and even negative m . These are associated to real spherical harmonics $Y_{l,2\mu} \propto \sin(2\mu\phi)$, $\mu = 1, 2, \dots, (l-1)/2$. Due to the $\sin(2\mu\phi)$ dependence, such contributions vanish upon integration over p_x or p_y , and thus the NoDES signal is washed out in standard VMI projections. While the NoDES signal can be recovered by doing full 3D reconstructions of the PAD, such reconstructions can be quite demanding. In Ref. [52] it was suggested to project the PAD along the $\hat{x} + \hat{y}$ direction, to avoid washing out the NoDES signal. However, such projection mixes the NoDES contributions (P_{YN}) with the other three (P_{NN} , P_{YY} , P_{NY}). Here we show that by taking the difference between the $\hat{x} + \hat{y}$ projection and the $\hat{x} - \hat{y}$ projection, one can reveal a pure NoDES signal. In practice, instead of projecting on two different directions, one rotates the

field polarization with respect to the VMI detector, which leads to a corresponding rotation of the PAD. Thus, our approach is the following: For the first (second) projection, the field is rotated by $\pi/4$ ($-\pi/4$) radians around the z axis, and the projection of the rotated PAD is done along y . This yields $P_{\pm\pi/4}(p_x, p_z)$. The difference of the two projections is taken as $\Delta P(p_x, p_z) \equiv [P_{\pi/4}(p_x, p_z) - P_{-\pi/4}(p_x, p_z)]/2$. The 2D NoDES signal $P_{\text{NoDES}}(p_x, p_z)$ can be extracted from the forward-backward asymmetric part of $\Delta P(p_x, p_z)$, i.e. $P_{\text{NoDES}}(p_x, p_z) \equiv [\Delta P(p_x, p_z) - \Delta P(p_x, -p_z)]/2$. To see this, consider the rotated distributions projected along p_y

$$\begin{aligned} P_{\pm\pi/4}(p_x, p_z) &\equiv \int_{-\infty}^{\infty} dp_y C_{8z}^{\pm} P(p_x, p_y, p_z) \\ &= \sum_{l,m} \int_{-\infty}^{\infty} dp_y b_{l,m}(p) Y_{l,m}(\theta, \phi \mp \frac{\pi}{4}), \end{aligned} \quad (6)$$

where C_{8z}^{\pm} is the operator that rotates functions by $\pm\pi/4$ around the z axis. The spherical harmonics can be written as $Y_{l,m}(\theta, \phi) = \mathcal{P}_{l,|m|}(\cos\theta)G_m(\phi)$, where $\mathcal{P}_{l,|m|}(\cos\theta)$ are (suitably normalized) generalized Legendre functions and $G_0(\phi) = 1$, $G_{|m|}(\phi) = \cos(|m|\phi)$ and $G_{-|m|} = \sin(|m|\phi)$. Therefore, the difference between the rotated PADs is given by

$$\Delta P(p_x, p_z) = \sum_{l,m} \int_{-\infty}^{\infty} dp_y b_{l,m}(p) \mathcal{P}_{l,|m|}(\cos\theta) \Delta G_m(\phi), \quad (7)$$

where $\Delta G_m(\phi) \equiv [G_m(\phi - \pi/4) - G_m(\phi + \pi/4)]/2$. Since $p = \sqrt{p_x^2 + p_y^2 + p_z^2}$ and $\cos\theta = p_z/p$ are even functions of p_y , the parity of the integrand is determined by $\Delta G_m(\phi)$, which is given by

$$\Delta G_m(\phi) = \begin{cases} \sin\left(\frac{m\pi}{4}\right) \sin(m\phi) & m > 0 \\ 0, & m = 0 \\ \sin\left(\frac{m\pi}{4}\right) \cos(m\phi) & m < 0 \end{cases} \quad (8)$$

Polar plots of $\sin(m\phi)$ and $\cos(m\phi)$ show that they are odd and even in p_y , respectively. Thus, integrals of $m > 0$ terms in the expression for $\Delta P(p_x, p_z)$ vanish, and only $m < 0$ terms contribute to $\Delta P(p_x, p_z)$ (except multiples of 4). Looking at Tables I and III, we see that $\Delta P(p_x, p_z)$ only contains contributions from P_{NY} and P_{YN} , which contain $m < 0$ terms. Furthermore, since P_{NY} and P_{YN} contributions are respectively even and odd in p_z , according to their characters with respect to σ_{xy} in Tables I and III, it follows that

$$\begin{aligned} P_{\text{NoDES}}(p_x, p_z) &\equiv \frac{1}{2} [\Delta P(p_x, p_z) - \Delta P(p_x, -p_z)] \\ &= \int_{-\infty}^{\infty} dp_y \Delta P_{YN}(p_x, p_y, p_z) \end{aligned} \quad (9)$$

where $\Delta P_{YN} \equiv (C_{8z}^+ P_{YN} - C_{8z}^- P_{YN})/2$ depends exclusively on the P_{YN} (NoDES) contribution. We demonstrate this approach for multiphoton and strong-field ionizations with orthogonal two-color fields in the numerical

$l \setminus m$	-9	-8	-7	-6	-5	-4	-3	-2	-1	0	1	2	3	4	5	6	7	8	9
0										NN									
1									NY										
2										NN	YY	NN							
3								NY	YN	NY									
4										NN	YY	NN	YY	NN					
5					NY	YN	NY	YN	NY										
6										NN	YY	NN	YY	NN	YY	NN			
7				NY	YN	NY	YN	NY	YN	NY									
8										NN	YY	NN	YY	NN	YY	NN	YY	NN	
9	NY	YN	NY	YN	NY	YN	NY	YN	NY										

Table IV. Enantiosensitivity (Y=Yes, N=No) and dichroism (Y/N) of the $b_{l,m}$ coefficients [see Eq. (4) and Table III] obtained upon ionization of randomly oriented chiral molecules with an orthogonal two-color field [Eq. (5)] for $l \leq 9$. See numerical confirmation in Sec. VI and experimental evidence in the companion paper [53].

simulations in Sec. VI, and experimentally in the companion paper [53].

V. PERTURBATION THEORY: RESONANTLY ENHANCED TWO-PHOTON IONIZATION OF METHYLOXIRANE

The selection rules derived in Sections II and III allow the emergence of NoDES terms, but do not provide information on their magnitude. In this section, we consider the scheme initially proposed in [52], i.e. two-photon ionization using a linearly polarized ultraviolet pulse and its orthogonally polarized second harmonic. We consider methyloxirane, a molecule where PECD has been exten-

sively studied [44, 56–61]. The energy difference between ground and first excited electronic states is $\Delta E = 7.12$ eV [62], while the ionization energy from the ground state is $I_p = 10.4$ eV [57]. Thus, two-photon resonantly enhanced ionization $|0\rangle \xrightarrow{2\omega} |1\rangle \xrightarrow{\omega} |k\rangle$ using $2\omega = 7.12$ eV and $\omega = 3.56$ eV ($\lambda = 348$ nm) leads to photoelectrons with kinetic energy $E_k = -I_p + 2\omega + \omega = 0.28$ eV. We model the excitation using the highest occupied and lowest unoccupied molecular orbitals (HOMO and LUMO) to represent the states $|0\rangle$ and $|1\rangle$, respectively. We neglect the contribution from all other non-resonant intermediate states, assume a fixed-nuclei approximation, and use second-order perturbation theory. Under these approximations, the value of $b_{3,-2}/b_{0,0}$ depends only on the transition dipoles and is given by [23, 52]

$$\frac{b_{3,-2}}{b_{0,0}} = \frac{1}{4} \sqrt{\frac{15}{7}} \frac{\int d\Omega_k \left[\hat{k} \cdot \left(\vec{d}_{1,0} \times \vec{d}_{k,1}^* \right) \right] \left[5 \left(\hat{k} \cdot \vec{d}_{k,1} \right) \left(\hat{k} \cdot \vec{d}_{1,0} \right) - \left(\vec{d}_{k,1} \cdot \vec{d}_{1,0} \right) \right]}{\int d\Omega_k \left(2 \left| \vec{d}_{k,1} \right|^2 \left| \vec{d}_{1,0} \right|^2 - \left| \vec{d}_{k,1} \cdot \vec{d}_{1,0} \right|^2 \right)}, \quad (10)$$

where $\vec{d}_{1,0} \equiv \langle 1|\vec{d}|0\rangle$ and $\vec{d}_{k,1}^* \equiv \langle \vec{k}|\vec{d}|1\rangle$ are the relevant transition dipoles, $|\vec{k}\rangle$ is the scattering state describing a photoelectron with momentum $\vec{p} = \hbar\vec{k}$ in the molecular frame, \hat{k} is the unit vector in the direction of \vec{k} , and $\int d\Omega_k$ is an integral over all photoelectron directions. This expression was derived using the approach presented in Ref. [23]. Note that in the framework of lowest-order perturbation theory used here, $b_{3,-2}$ does not depend on φ [52].

We calculated the transition dipoles using state-of-the-art methods [63–65], which often lead to quantitative agreement with PECD experiments. We also consider the process $|0\rangle \xrightarrow{\omega} |1\rangle \xrightarrow{2\omega} |k\rangle$ using $\omega = 7.12$ eV ($\lambda = 174$ nm), which leads to photoelectrons with kinetic energy $E_k = -I_p + 2\omega + \omega = 10.96$ eV. Note that changing the photon ordering also induces an extra minus sign in Eq. (10), see Appendix E of Ref. [23]. Figure 1 shows $b_{3,-2}/b_{0,0}$ for a few values of the photoelectron

kinetic energy in low and high photoelectron energy regions. $b_{3,-2}/b_{0,0}$ is of the order of 1% in both regions, which is similar to the ratio $b_{1,0}/b_{0,0}$ reached in multiphoton PECD of methyloxirane [44], and is considerably higher than traditional CD chiroptical signals ($\sim 0.01\%$ [66]). Since the value of $b_{3,-2}/b_{0,0}$ is highly dependent on the transition dipole matrix elements, exploring different intermediate states and final photoelectron energies can potentially enhance it [18]. We have not attempted such optimization.

VI. TDSE CALCULATIONS: MULTIPHOTON AND STRONG-FIELD IONIZATIONS OF A TOY-MODEL CHIRAL MOLECULE

In this section, we analyze the emergence of NoDES structures in the multiphoton and strong-field ionization

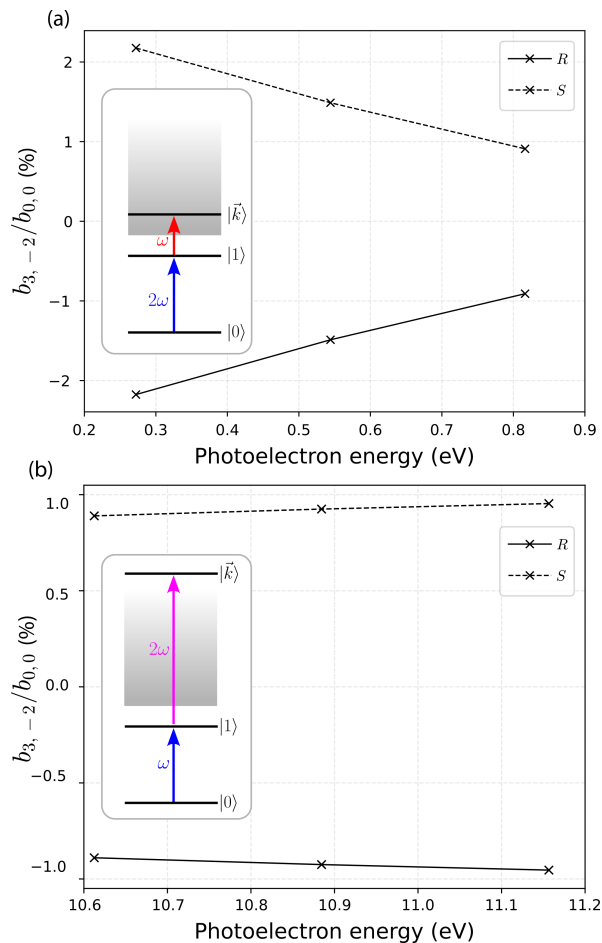


Figure 1. Perturbation-theory calculations for the lowest NoDES contribution $b_{3,-2}$ normalized to the total yield $b_{0,0}$ [Eq. (10)] as a function of the photoelectron energy in two-photon resonantly enhanced ionization of methyloxirane with an orthogonal two-color field [Eq. (5)] for two different photon orderings. In (a) $\omega = 3.56$ eV while in (b) $\omega = 7.12$ eV. The ground and intermediate states are described by the HOMO and LUMO orbitals.

regimes where the perturbative approach becomes impractical. We thus model the interaction by direct integration of the Time-Dependent Schrödinger Equation (TDSE) for a toy-model chiral molecule with ionization potential $I_p = 8.98$ eV, as detailed in [16]. Despite the simplicity of the molecular structure (made of four nuclei and one electron), this model was shown to produce signals qualitatively resembling the results of experiments performed in fenchone, in various field configurations (orthogonal two-color bilinear fields [16, 51], co-rotating [19] and counter-rotating [20] two-color bicircular fields). Here we let the molecule interact with a fundamental 800 nm laser field of intensity I and an orthogonally polarized 400 nm laser field, with an amplitude ratio $r = 30\%$ and a phase shift φ between the two components of the electric field. The laser pulse duration is four cycles of the fundamental, with one-cycle

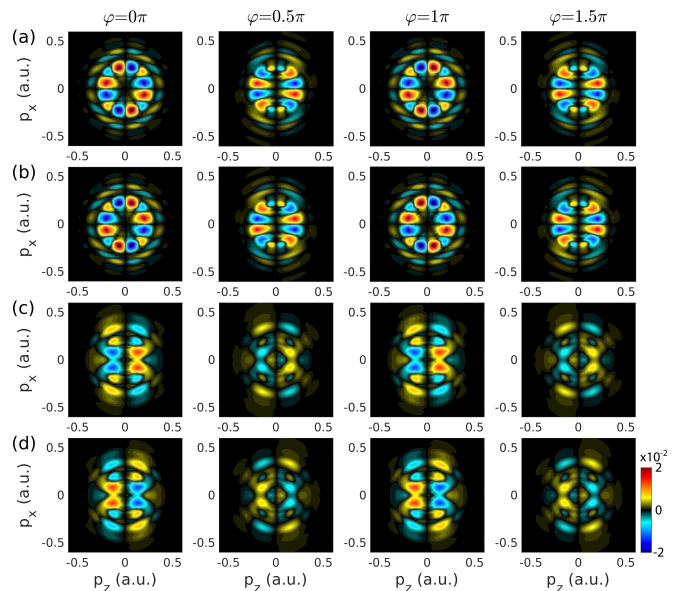


Figure 2. TDSE calculations of the photoionization of a toy-model chiral molecule by an orthogonally polarized two-color laser field at various relative phases φ [Eq. (5)]. The intensity of the 800 nm fundamental field component is $I = 5 \times 10^{12}$ W/cm² so that the interaction lies in the multiphoton regime. (a-b) Projections of the forward-backward antisymmetric part of the PAD along the \hat{y} direction, in one enantiomer (a) and its mirror image (b). (c-d) NoDES signal obtained by subtracting the $\hat{x} + \hat{y}$ and $\hat{x} - \hat{y}$ projections of the forward-backward antisymmetric part of the PAD (see Sec. IV), in one enantiomer (c) and its mirror image (d).

ascending and descending ramps. The short duration induces carrier-envelope dependent effects, whose influence is canceled by appropriate symmetrization of the photoelectron distributions, as detailed in [16]. The calculation is averaged over random molecular orientations to obtain the final photoelectron momentum distribution. Practical details on the numerical recipe can be found in [16]. As in PECD, the chiral potential induces an FBA in the electron scattering process, and the enantiosensitive part of the PAD is thus obtained by extracting the FBA: $A(p_x, p_y, p_z) = \frac{1}{2} [P(p_x, p_y, p_z) - P(p_x, p_y, -p_z)]$.

We first consider the case of a fundamental 800 nm field with $I = 5 \times 10^{12}$ W/cm². The Keldysh parameter associated to the interaction is $\gamma = 3.9$, which is characteristic of the multiphoton ionization regime. Figure 2 (a,b) shows projections of the FBA in the (x, z) plane as a function of φ , obtained in the two enantiomers of the chiral molecule. The FBA is up-down antisymmetric, reflecting the C_{2y} symmetry of the field and the switch of the effective laser ellipticity every half laser period, as predicted and observed in previous studies [16, 49], as well as in the measurements reported in [53]. The FBA changes sign when switching enantiomer, and also when the phase between the two colors is shifted by π , i.e. when the ellipticity of the ionizing field reverses. The observed signal is thus enantiosensitive and dichroic. In-

deed, the non-dichroic part of the enantiosensitive signal is expected to cancel out in the projection along the \hat{y} direction. To reveal it, we follow the method presented in Sec. IV, and used in the experiment in the companion paper [53]. We project the FBA along the $\hat{x} + \hat{y}$ and $\hat{x} - \hat{y}$ directions, and plot half the difference between the two projections. The results (Fig. 2(c,d)) show a significant FBA, in the 1% range of the maximum electron yield, and keep a constant sign upon shifting φ by π . This term is thus non-dichroic. Comparing the results obtained in opposite enantiomers shows that it changes sign, confirming that this procedure enables detecting the NoDES component.

The spherical harmonic decomposition of the 3D PAD should give direct access to the NoDES terms. We thus apply the fitting procedure [67] used for experimental strong-field PEELD distributions in [53], to the simulated distributions. Figure 3 shows the coefficients of the different spherical harmonics as a function of φ in both enantiomers as well as the enantiodifferential coefficients. The decomposition was performed using $l_{max} = 9$. The $l \neq 0$ coefficients are normalized by $b_{0,0}$. The distribution shows two classes of terms, with different orders of magnitude: the even $m \geq 0$ terms and the odd $m < 0$ ones are dominant, while the odd $m > 0$ terms and the even $m < 0$ ones are two orders of magnitude weaker. Switching enantiomer (Fig. 3 (a-b)) leaves the former terms unchanged and changes the sign of the latter. The enantiosensitive terms are isolated in the enantiodifferential signals (Fig. 3 (c)). The odd $m > 0$ components oscillate around zero as a function of φ , changing sign when φ is shifted by π . These terms are thus dichroic. By contrast almost all the $m < 0$ terms show a constant sign as a function of φ . Some components, like the low-momentum part of $b_{5,-2}$, change sign as a function of φ , but with a double periodicity: they switch sign when φ is shifted by $\pi/2$, and thus have the same sign when φ changes by π . These terms are thus non-dichroic. The sign changes they may show is related to the change in the shape of the laser field, which evolves from a ‘‘C’’ shape at $\varphi = 0$ to a ‘‘8’’ shape at $\varphi = \pi/2$. Thus, the enantiosensitivity and dichroic nature of the different spherical harmonic coefficients we found in these simulations confirms the symmetry analysis leading to Table IV.

Next, we consider an 800 nm laser field with intensity $I = 5 \times 10^{13}$ W/cm² to enter the strong-field ionization regime. The Keldysh parameter associated to the interaction is now $\gamma = 1.2$, which is characteristic of (non-adiabatic) tunneling ionization processes. Fig. 4(a,b) presents the projections of the FBA along the \hat{y} direction as a function of φ , for the two enantiomers of the toy-model molecule. The FBA is stretched along the x direction compared to the multiphoton case of Fig. 2 and exhibits higher above-threshold ionization peaks. This is consistent with strong-field driven electron dynamics. The FBA is up-down antisymmetric, following the sub-cycle ellipticity of the two-color laser field and its C_{2y} symmetry, and it changes sign when the phase φ is in-

creased by π . It also changes sign when the enantiomeric form of the molecular sample is reversed. Therefore, the whole FBA, projected along y , is dichroic and enantiosensitive, as in the multiphoton case. We implemented again the procedure presented in Sec. IV to isolate the NoDES signal. The results are presented in Fig. 4(c,d) for both enantiomers and varying φ . The non-dichroic nature of the signal shows up through the up-down symmetry of all the results and their insensitivity to $\varphi \rightarrow \varphi + \pi$. The enantiosensitivity corresponds to the antisymmetry of the graphs displayed in Fig. 4(c) and Fig. 4(d). Beyond its insensitivity to $\varphi \rightarrow \varphi + \pi$ phase variation, the NoDES signal does not depend as strongly as the rest of the FBA on smaller variations of φ , as evidenced in Fig. 4 through the comparison of FBA and NoDES results at $\varphi = 0$ and $\varphi = \pi/2$.

Finally, we undertook spherical harmonic decompositions of the 3D PADs associated to the strong-field interaction. The results are presented in Fig. 5 for the toy-model molecule (a), its mirror image (b) and their differences in (c). The results are again fully consistent with Table IV derived from symmetry arguments: the PAD consist of even l , $m \geq 0$ and odd l , $m < 0$ components. Within the former group, the non-dichroic and non-enantiosensitive coefficients, $b_{l,m}$ with even l and m , have a larger relative contribution to the PAD in the strong-field regime than in the case of multiphoton ionization (see e.g. $b_{6,m \geq 0}$ in Fig. 3 (a) and Fig. 5(a)). Within the odd l , $m < 0$ group, the dichroic and non-enantiosensitive components, $b_{l,m}$ with odd l and m , also exhibit a larger magnitude with respect to the NoDES ones in the strong-field configuration (see e.g. $b_{7,m < 0}$ in Fig. 3 (a) and Fig. 5(a)). This may be due to the fact that the electric field progressively inhibits the role of the ionic potential in the electron dynamics as the field intensity increases. However, the NoDES contributions, $b_{l,m}$ with odd l and even m , still present significant ($\sim 1\%$) magnitude, up to rather high photoelectron kinetic energies and large angular momenta.

VII. CONCLUSIONS

We have shown how the symmetry properties of elliptical and orthogonal two-color fields interacting with randomly oriented chiral molecules leads to photoelectron angular distributions that can be decomposed into four irreducible representations of the D_{2h} point group. One of these representations, A_u , describes a component of the photoelectron angular distribution that changes sign when the enantiomer is replaced by its mirror image, but not when the ellipticity of the field is reversed. This non-dichroic enantiosensitive (NoDES) component enables the detection of molecular chirality in a way that is robust against variations in the relative phase between orthogonal field components. Since this robustness stems from the symmetry properties of the system, NoDES signals are an example of symmetry protection, as observed

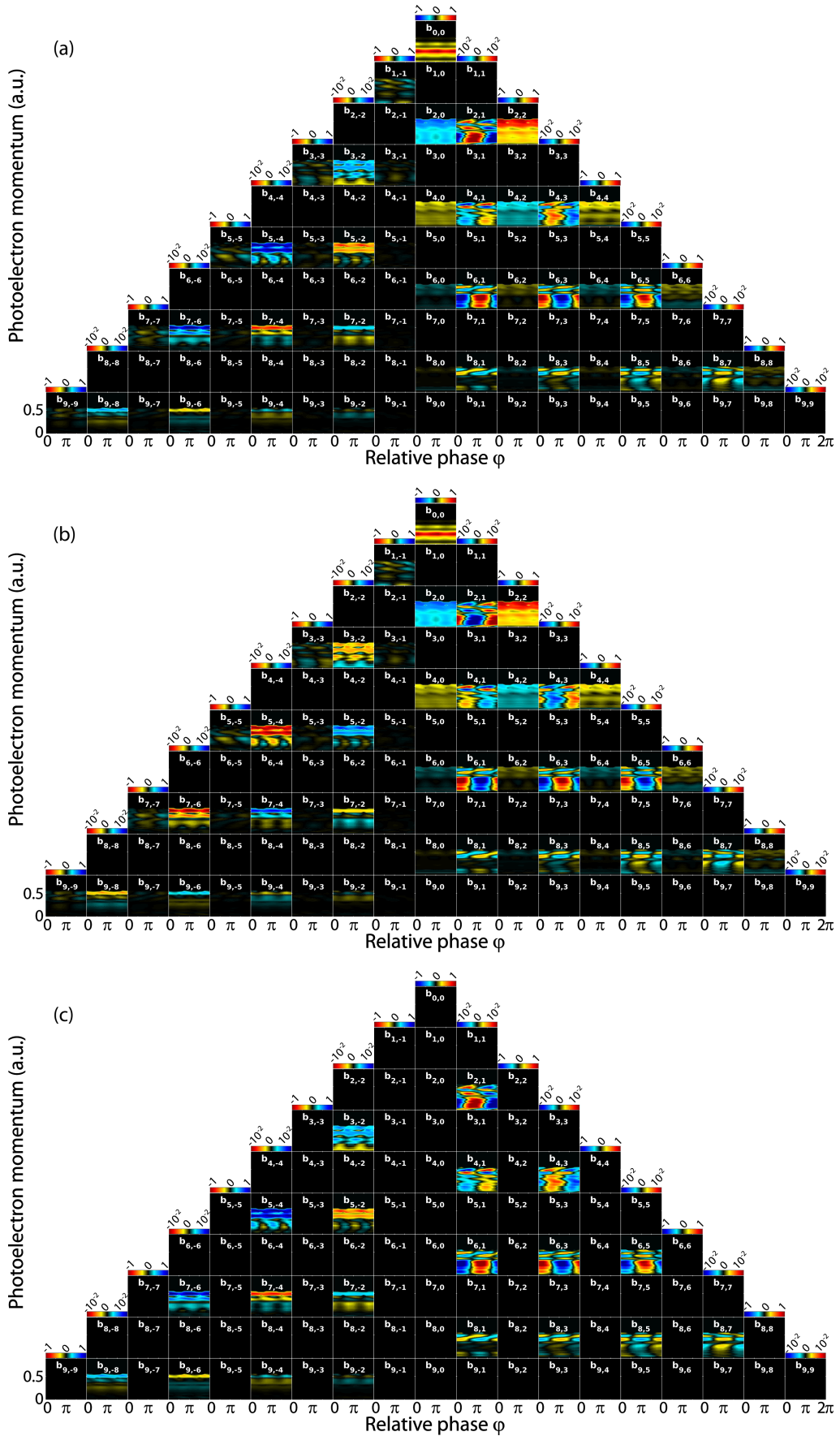


Figure 3. Spherical harmonic decomposition of the photoelectron angular distributions obtained by TDSE simulations of the photoionization of a toy-model chiral molecule (first enantiomer in (a), second enantiomer in (b)) by an orthogonal two-color field at $5 \times 10^{12} \text{ W/cm}^2$. The enantiodifferential, forward-backward antisymmetric signal is shown in (c).

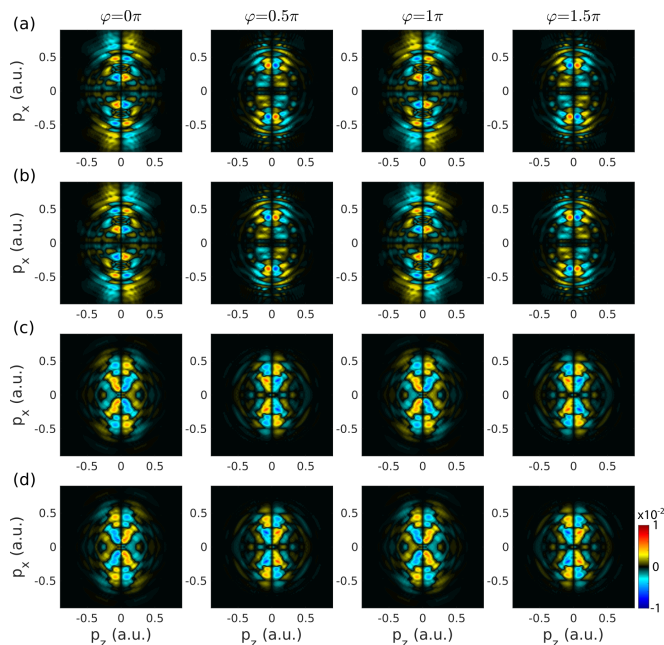


Figure 4. Same as Fig. 2 but for $I = 5 \times 10^{13}$ W/cm² so that the interaction lies in the strong-field regime.

in other fields of physics [68, 69], in the context of chiroptical spectroscopy.

We have provided a measurement protocol to extract the NoDES component of the photoelectron angular distribution, without background from the other components, using only two velocity-map imaging projections. This protocol has been tested both on numerical simulations here, and on experimental data in the companion paper [53].

We have quantified the magnitude of the NoDES sig-

nal for orthogonal two-color fields in perturbative two-photon, multiphoton and strong-field ionization regimes, and found that it is of the order of 1% of the energy-resolved ionization yield. This order of magnitude is in agreement with the experimental data in the companion paper [53]. Furthermore, this magnitude is comparable to that of photoelectron circular dichroism in the strong-field regime, and thus much bigger than standard chiroptical effects relying on magnetic-dipole interactions, which are typically below 0.1% [66]. Therefore, NoDES spectroscopy can be used to image molecular chirality on the ultrafast electronic time scale in a broad range of ionization regimes, and in the absence of a fixed relative phase between the orthogonal field components.

ACKNOWLEDGMENTS

We acknowledge Valérie Blanchet and Baptiste Fabre for fruitful discussions. A. O. acknowledges funding from the Deutsche Forschungsgemeinschaft (DFG, German Research Foundation) - 543760364. D.A. acknowledges funding from the Royal Society URF\R\251036. This work is part of the ULTRAFast and TORNADO projects of PEPR LUMA and was supported by the French National Research Agency, under grant under ANR-21-CE30-038-01 (Shotime), and as a part of the France 2030 program, under grants ANR-23-EXLU-0002 and ANR-23-EXLU-0004. We acknowledge the financial support of the IdEx University of Bordeaux / Grand Research Program “GPR LIGHT”. This project has received funding from European Union’s Horizon 2020 research and innovation programme under grant agreement no. 871124 Laserlab-Europe. The ELI ALPS project (GINOP-2.3.6-15-2015-00001) is supported by the European Union and co-financed by the European Regional Development Fund.

-
- [1] N. Berova, P. L. Polavarapu, K. Nakanishi, and R. W. Woody, *Comprehensive Chiroptical Spectroscopy* (Wiley, Hoboken, New Jersey, 2012).
- [2] J. Kumar, T. Nakashima, and T. Kawai, Circularly polarized luminescence in chiral molecules and supramolecular assemblies, *The Journal of Physical Chemistry Letters* **6**, 3445–3452 (2015).
- [3] G. L. J. A. Rikken and E. Raupach, Observation of magneto-chiral dichroism, *Nature* **390**, 493–494 (1997).
- [4] B. Ritchie, Theory of the angular distribution of photoelectrons ejected from optically active molecules and molecular negative ions, *Physical Review A* **13**, 1411 (1976).
- [5] I. Powis, Photoelectron circular dichroism of the randomly oriented chiral molecules glyceraldehyde and lactic acid, *The Journal of Chemical Physics* **112**, 301 (2000).
- [6] C. Sparling and D. Townsend, Two decades of imaging photoelectron circular dichroism: From first principles to future perspectives, *Physical Chemistry Chemical Physics* **27**, 2888 (2025).
- [7] A. Comby, S. Beaulieu, M. Boggio-Pasqua, D. Descamps, F. Légaré, L. Nahon, S. Petit, B. Pons, B. Fabre, Y. Mairesse, and V. Blanchet, Relaxation Dynamics in Photoexcited Chiral Molecules Studied by Time-Resolved Photoelectron Circular Dichroism: Toward Chiral Femtochemistry, *The Journal of Physical Chemistry Letters* **7**, 4514 (2016).
- [8] V. Wanie, E. Bloch, E. P. Månsson, L. Colaizzi, S. Ryabchuk, K. Saraswathula, A. F. Ordonez, D. Ayuso, O. Smirnova, A. Trabattini, *et al.*, Capturing electron-driven chiral dynamics in UV-excited molecules, *Nature* **630**, 109 (2024).
- [9] L. Nahon, G. A. Garcia, and I. Powis, Valence shell one-photon photoelectron circular dichroism in chiral systems, *Journal of Electron Spectroscopy and Related Phenomena Gas Phase Spectroscopic and Dynamical Studies at Free-Electron Lasers and Other Short Wavelength Sources*, **204**, Part B, 322 (2015).

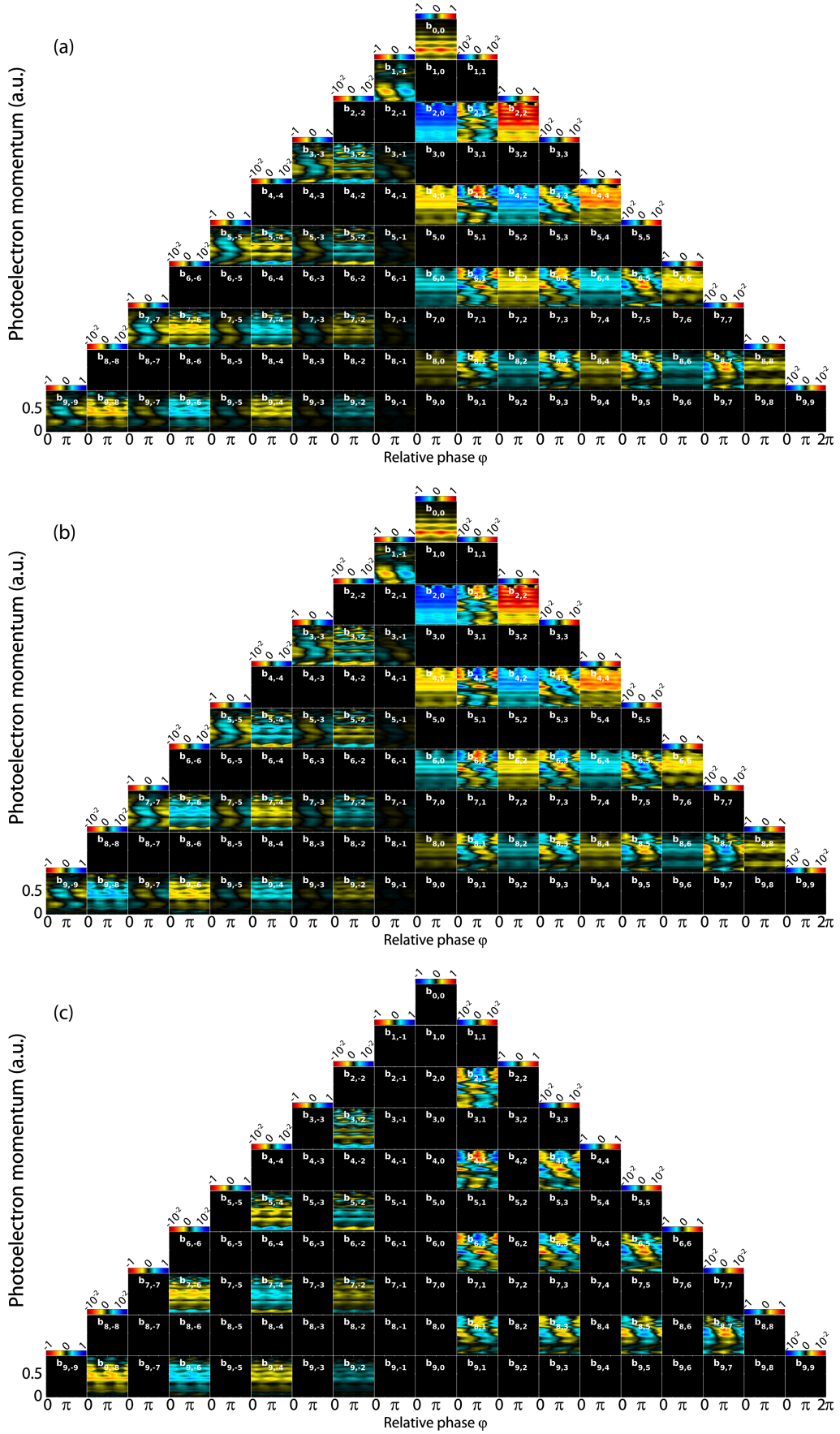


Figure 5. Same as Fig. 3 but for $I = 5 \times 10^{13} \text{ W/cm}^2$.

- [10] S. Beaulieu, A. Ferré, R. Géneaux, R. Canonge, D. Descamps, B. Fabre, N. Fedorov, F. Légaré, S. Petit, T. Ruchon, V. Blanchet, Y. Mairesse, and B. Pons, Universality of photoelectron circular dichroism in the photoionization of chiral molecules, *New Journal of Physics* **18**, 102002 (2016).
- [11] H.-g. Lee, S. T. Ranecky, S. Vasudevan, N. Ladda, T. Rosen, S. Das, J. Ghosh, H. Braun, D. M. Reich, A. Senftleben, and T. Baumert, Pulse length dependence of photoelectron circular dichroism, *Physical Chemistry Chemical Physics* **24**, 27483 (2022).
- [12] N. Böwering, T. Lischke, B. Schmidtke, N. Müller, T. Khalil, and U. Heinzmann, Asymmetry in Photoelectron Emission from Chiral Molecules Induced by Circularly Polarized Light, *Physical Review Letters* **86**, 1187 (2001).
- [13] C. Lux, M. Wollenhaupt, T. Bolze, Q. Liang, J. Köhler, C. Sarpe, and T. Baumert, Circular Dichroism in the Photoelectron Angular Distributions of Camphor and Fenchone from Multiphoton Ionization with Femtosecond Laser Pulses, *Angewandte Chemie International Edition* **51**, 5001 (2012).
- [14] C. S. Lehmann, N. B. Ram, I. Powis, and M. H. M. Janssen, Imaging photoelectron circular dichroism of chiral molecules by femtosecond multiphoton coincidence detection, *The Journal of Chemical Physics* **139**, 234307 (2013).
- [15] S. Beaulieu, A. Comby, A. Clergerie, J. Caillat, D. Descamps, N. Dudovich, B. Fabre, R. Géneaux, F. Légaré, S. Petit, B. Pons, G. Porat, T. Ruchon, R. Taïeb, V. Blanchet, and Y. Mairesse, Attosecond-resolved photoionization of chiral molecules, *Science* **358**, 1288 (2017).
- [16] S. Rozen, A. Comby, E. Bloch, S. Beauvarlet, D. Descamps, B. Fabre, S. Petit, V. Blanchet, B. Pons, N. Dudovich, and Y. Mairesse, Controlling Subcycle Optical Chirality in the Photoionization of Chiral Molecules, *Physical Review X* **9**, 031004 (2019).
- [17] R. E. Goetz, C. P. Koch, and L. Greenman, Perfect control of photoelectron anisotropy for randomly oriented ensembles of molecules by XUV REMPI and polarization shaping, *The Journal of Chemical Physics* **151**, 074106 (2019).
- [18] R. E. Goetz, C. P. Koch, and L. Greenman, Quantum control of photoelectron circular dichroism, *Physical Review Letters* **122**, 013204 (2019).
- [19] E. Bloch, S. Larroque, S. Rozen, S. Beaulieu, A. Comby, S. Beauvarlet, D. Descamps, B. Fabre, S. Petit, R. Taïeb, A. J. Uzan, V. Blanchet, N. Dudovich, B. Pons, and Y. Mairesse, Revealing the Influence of Molecular Chirality on Tunnel-Ionization Dynamics, *Physical Review X* **11**, 041056 (2021).
- [20] S. Beaulieu, S. Larroque, D. Descamps, B. Fabre, S. Petit, R. Taïeb, B. Pons, and Y. Mairesse, Strong-field ionization of chiral molecules with bicircular laser fields: Sub-barrier dynamics, interference, and vortices, *Physical Review A* **110**, 013103 (2024).
- [21] M. Hofmann, D. Trabert, A. Geyer, N. Anders, J. Kruse, J. Rist, L. P. H. Schmidt, T. Jahnke, M. Kunitzki, M. S. Schöffler, S. Eckart, and R. Dörner, Sub-cycle resolved strong field ionization of chiral molecules and the origin of chiral photoelectron asymmetries [10.48550/arXiv.2402.03215](https://arxiv.org/abs/10.48550/arXiv.2402.03215) (2024), [arXiv:2402.03215](https://arxiv.org/abs/2402.03215).
- [22] D. Ayuso, A. F. Ordonez, and O. Smirnova, Ultrafast chirality: The road to efficient chiral measurements, *Physical Chemistry Chemical Physics* **24**, 26962 (2022).
- [23] A. F. Ordonez and O. Smirnova, A geometric approach to decoding molecular structure and dynamics from photoionization of isotropic samples, *Physical Chemistry Chemical Physics* **24**, 13605 (2022).
- [24] M. Bashkansky, P. H. Bucksbaum, and D. W. Schumacher, Asymmetries in Above-Threshold Ionization, *Physical Review Letters* **60**, 2458 (1988).
- [25] S. Basile, F. Trombetta, and G. Ferrante, Twofold Symmetric Angular Distributions in Multiphoton Ionization with Elliptically Polarized Light, *Physical Review Letters* **61**, 2435 (1988).
- [26] H. G. Muller, G. Petite, and P. Agostini, Comment on “Asymmetries in Above-Threshold Ionization”, *Physical Review Letters* **61**, 2507 (1988).
- [27] P. Lambropoulos and X. Tang, Comment on “Asymmetries in Above-Threshold Ionization”, *Physical Review Letters* **61**, 2506 (1988).
- [28] L. A. A. Nikolopoulos and P. Lambropoulos, Above-threshold ionization of negative hydrogen, *Physical Review A* **56**, 3106 (1997).
- [29] N. L. Manakov, A. Maquet, S. I. Marmo, V. Veniard, and G. Ferrante, Elliptic dichroism and angular distribution of electrons in two-photon ionization of atoms, *Journal of Physics B: Atomic, Molecular and Optical Physics* **32**, 3747 (1999).
- [30] Z.-M. Wang and D. S. Elliott, Determination of Cross Sections and Continuum Phases of Rubidium through Complete Measurements of Atomic Multiphoton Ionization, *Physical Review Letters* **84**, 3795 (2000).
- [31] B. Borca, M. V. Frolov, N. L. Manakov, and A. F. Starace, Threshold Effects on Angular Distributions for Multiphoton Detachment by Intense Elliptically Polarized Light, *Physical Review Letters* **87**, 133001 (2001).
- [32] S. P. Goreslavski, G. G. Paulus, S. V. Popruzhenko, and N. I. Shvetsov-Shilovski, Coulomb Asymmetry in Above-Threshold Ionization, *Physical Review Letters* **93**, 233002 (2004).
- [33] S. V. Popruzhenko, G. G. Paulus, and D. Bauer, Coulomb-corrected quantum trajectories in strong-field ionization, *Physical Review A* **77**, 053409 (2008).
- [34] W. Becker and D. B. Milošević, Elliptic dichroism in strong-field ionization of atoms subjected to tailored laser fields, *Physical Chemistry Chemical Physics* **24**, 7014 (2022).
- [35] M. Davino, E. McManus, P.-H. Tran, V.-H. Hoang, A. F. Ordóñez, G. Gibson, T. Saule, A.-T. Le, and C. A. Trallero-Herrero, Symmetries in three-dimensional photoelectron momentum spectroscopy as precursory methods for dichroic and enantiosensitive measurements, *Physical Review Applied* **23**, 014022 (2025).
- [36] C. Lux, M. Wollenhaupt, C. Sarpe, and T. Baumert, Photoelectron Circular Dichroism of Bicyclic Ketones from Multiphoton Ionization with Femtosecond Laser Pulses, *ChemPhysChem* **16**, 115 (2015).
- [37] J. Miles, D. Fernandes, A. Young, C. M. M. Bond, S. W. Crane, O. Ghafur, D. Townsend, J. Sá, and J. B. Greenwood, A new technique for probing chirality via photoelectron circular dichroism, *Analytica Chimica Acta* **984**, 134 (2017).
- [38] A. Comby, E. Bloch, C. M. M. Bond, D. Descamps, J. Miles, S. Petit, S. Rozen, J. B. Greenwood, V. Blanchet, and Y. Mairesse, Real-time determination

- of enantiomeric and isomeric content using photoelectron elliptical dichroism, *Nature Communications* **9**, 5212 (2018).
- [39] C. Sparling, A. Ruget, L. Ireland, N. Kotsina, O. Ghafur, J. Leach, and D. Townsend, The importance of molecular axis alignment and symmetry-breaking in photoelectron elliptical dichroism, *The Journal of Chemical Physics* **159**, 214301 (2023).
- [40] J. B. Greenwood and I. D. Williams, Investigation of photoelectron elliptical dichroism for chiral analysis, *Physical Chemistry Chemical Physics* **25**, 16238 (2023).
- [41] S. Beauvarlet, E. Bloch, D. Rajak, D. Descamps, B. Fabre, S. Petit, B. Pons, Y. Mairesse, and V. Blanchet, Photoelectron elliptical dichroism spectroscopy of resonance-enhanced multiphoton ionization via the 3s, 3p and 3d Rydberg series in fenchone, *Physical Chemistry Chemical Physics* **24**, 6415 (2022).
- [42] A. Comby, D. Descamps, S. Petit, E. Valzer, M. Wloch, L. Pouységu, S. Quideau, J. Bocková, C. Meinert, V. Blanchet, B. Fabre, and Y. Mairesse, Fast and precise chiroptical spectroscopy by photoelectron elliptical dichroism, *Physical Chemistry Chemical Physics* **25**, 16246 (2023).
- [43] A. T. J. B. Eppink and D. H. Parker, Velocity map imaging of ions and electrons using electrostatic lenses: Application in photoelectron and photofragment ion imaging of molecular oxygen, *Review of Scientific Instruments* **68**, 3477 (1997).
- [44] M. M. Rafiee Fanood, I. Powis, and M. H. M. Janssen, Chiral Asymmetry in the Multiphoton Ionization of Methyloxirane Using Femtosecond Electron–Ion Coincidence Imaging, *The Journal of Physical Chemistry A* **118**, 11541 (2014).
- [45] K. Fehre, S. Eckart, M. Kunitski, C. Janke, D. Trabert, J. Rist, M. Weller, A. Hartung, M. Pitzer, L. Ph. H. Schmidt, T. Jahnke, R. Dörner, and M. S. Schöffler, Angular streaking in strong field ionization of chiral molecules, *Physical Review Research* **1**, 033045 (2019).
- [46] M. Wollenhaupt, M. Krug, J. Köhler, T. Bayer, C. Sarpe-Tudoran, and T. Baumert, Three-dimensional tomographic reconstruction of ultrashort free electron wave packets, *Applied Physics B* **95**, 647 (2009).
- [47] C. Sparling and D. Townsend, Tomographic reconstruction techniques optimized for velocity-map imaging applications, *The Journal of Chemical Physics* **157**, 114201 (2022).
- [48] C. Sparling, D. Rajak, V. Blanchet, Y. Mairesse, and D. Townsend, Fourier–Hankel–Abel Nyquist-limited tomography: A spherical harmonic basis function approach to tomographic velocity-map image reconstruction, *Review of Scientific Instruments* **95**, 053301 (2024).
- [49] P. V. Demekhin, A. N. Artemyev, A. Kastner, and T. Baumert, Photoelectron Circular Dichroism with Two Overlapping Laser Pulses of Carrier Frequencies ω and 2ω Linearly Polarized in Two Mutually Orthogonal Directions, *Physical Review Letters* **121**, 253201 (2018).
- [50] P. V. Demekhin, Photoelectron circular dichroism with Lissajous-type bichromatic fields: One-photon versus two-photon ionization of chiral molecules, *Physical Review A* **99**, 063406 (2019).
- [51] S. Rozen, S. Larroque, N. Dudovich, Y. Mairesse, and B. Pons, Enhanced chiral-sensitivity of Coulomb-focused electrons in strong field ionization, *Journal of Physics B: Atomic, Molecular and Optical Physics* **54**, 184002 (2021).
- [52] A. F. Ordóñez and O. Smirnova, Disentangling enantiosensitivity from dichroism using bichromatic fields, *Physical Chemistry Chemical Physics* **24**, 7264 (2022).
- [53] L. Fede, D. Rajak, C. Sparling, D. Ayuso, V. Blanchet, P. Decleva, D. Decamps, S. Petit, B. Pons, Y. Mairesse, and A. Ordóñez, Non-dichroic enantio-sensitive chiroptical spectroscopy, arXiv (2025).
- [54] Y.-I. Suzuki, Chiral photoelectron spectroscopy using unpolarized light, *Physical Review A* **109**, L060802 (2024).
- [55] K. Fehre, N. M. Novikovskiy, S. Grundmann, G. Kastirke, S. Eckart, F. Trinter, J. Rist, A. Hartung, D. Trabert, C. Janke, G. Nalin, M. Pitzer, S. Zeller, F. Wiegandt, M. Weller, M. Kircher, M. Hofmann, L. P. H. Schmidt, A. Knie, A. Hans, L. B. Ltaief, A. Ehresmann, R. Berger, H. Fukuzawa, K. Ueda, H. Schmidt-Böcking, J. B. Williams, T. Jahnke, R. Dörner, M. S. Schöffler, and P. V. Demekhin, Fourfold differential photoelectron circular dichroism, *Physical Review Letters* **127**, 103201 (2021).
- [56] M. Stener, G. Fronzoni, D. D. Tommaso, and P. Decleva, Density functional study on the circular dichroism of photoelectron angular distribution from chiral derivatives of oxirane, *The Journal of Chemical Physics* **120**, 3284 (2004).
- [57] S. Stranges, S. Turchini, M. Alagia, G. Alberti, G. Contini, P. Decleva, G. Fronzoni, M. Stener, N. Zema, and T. Prosperi, Valence photoionization dynamics in circular dichroism of chiral free molecules: The methyl-oxirane, *The Journal of Chemical Physics* **122**, 244303 (2005).
- [58] D. D. Tommaso, M. Stener, G. Fronzoni, and P. Decleva, Conformational Effects on Circular Dichroism in the Photoelectron Angular Distribution, *ChemPhysChem* **7**, 924 (2006).
- [59] G. Contini, N. Zema, S. Turchini, D. Catone, T. Prosperi, V. Carravetta, P. Bolognesi, L. Avaldi, and V. Feyer, Vibrational state dependence of β and D asymmetry parameters: The case of the highest occupied molecular orbital photoelectron spectrum of methyl-oxirane, *The Journal of Chemical Physics* **127**, 124310 (2007).
- [60] G. A. Garcia, L. Nahon, S. Daly, and I. Powis, Vibrationally induced inversion of photoelectron forward-backward asymmetry in chiral molecule photoionization by circularly polarized light, *Nature Communications* **4**, 2132 (2013).
- [61] G. A. Garcia, H. Dossmann, L. Nahon, S. Daly, and I. Powis, Identifying and Understanding Strong Vibronic Interaction Effects Observed in the Asymmetry of Chiral Molecule Photoelectron Angular Distributions, *ChemPhysChem* **18**, 500 (2017).
- [62] D. Cohen, M. Levi, H. Basch, and A. Gedanken, Excited electronic states of optically active substituted ethylene oxides: (-)-(S)-2-methyloxirane and (-)-(S,S)-2,3-dimethyloxirane, *Journal of the American Chemical Society* **105**, 1738 (1983).
- [63] D. Toffoli, M. Stener, G. Fronzoni, and P. Decleva, Convergence of the multicenter B-spline DFT approach for the continuum, *Chemical Physics* **276**, 25 (2002).
- [64] S. Stranges, S. Turchini, M. Alagia, G. Alberti, G. Contini, P. Decleva, G. Fronzoni, M. Stener, N. Zema, and T. Prosperi, Valence photoionization dynamics in circular dichroism of chiral free molecules: The methyl-oxirane, *The Journal of Chemical Physics* **122**, 244303 (2005).
- [65] D. Toffoli, S. Coriani, M. Stener, and P. Decleva, Tire-

- sia: A code for molecular electronic continuum states and photoionization, [Computer Physics Communications](#) , **109038** (2023).
- [66] H. Tanaka, Y. Inoue, and T. Mori, Circularly Polarized Luminescence and Circular Dichroisms in Small Organic Molecules: Correlation between Excitation and Emission Dissymmetry Factors, [ChemPhotoChem](#) **2**, 386 (2018).
- [67] A. Politis, *Microphone Array Processing for Parametric Spatial Audio Techniques* (Aalto University, 2016).
- [68] Y. Plotnik, O. Peleg, F. Dreisow, M. Heinrich, S. Nolte, A. Szameit, and M. Segev, Experimental Observation of Optical Bound States in the Continuum, [Physical Review Letters](#) **107**, 183901 (2011).
- [69] Z.-C. Gu and X.-G. Wen, Tensor-entanglement-filtering renormalization approach and symmetry-protected topological order, [Physical Review B](#) **80**, 155131 (2009).